Design Evaluation of A-PET: A High Sensitivity Animal PET Camera

S. Surti, *Member, IEEE,* J. S. Karp, *Senior Member, IEEE,* A. E. Perkins, *Member, IEEE,* R. Freifelder, *Member, IEEE,* and G. Muehllehner, *Fellow, IEEE*

***Abstract*—In recent years it has been shown that PET is capable of obtaining *in vivo* metabolic images of small animals. These serve as models to study the development and progress of diseases within humans. Imaging small animals requires not only image resolution better than 2 mm, but also high sensitivity in order to image ligands with low specific activity or radiochemical yields. Toward achieving these goals, we have developed a discrete $2 \times 2 \times 10\ \mathrm{mm}^3$ GSO Anger-logic detector for use in a high resolution, high sensitivity, and high count-rate animal PET scanner. This detector uses relatively large 19 mm diameter photomultiplier tubes (PMT), but nevertheless achieves good spatial and energy resolution. The scanner (A-PET) has a port diameter of 21 cm, transverse field-of-view of 12.8 cm, axial length of 11.6 cm, and operates in 3-D volume imaging mode. The absolute coincidence sensitivity is 1.3% for a point source. Due to the use of large PMTs in an Anger design, the encoding ratio (number of crystals/PMT) is high, which reduces the complexity and leads to a cost-effective scanner. Simulation results show that this scanner can achieve high NEC rates for small cylindrical phantoms due to its high sensitivity and low deadtime. Initial measurements show that our design goals for spatial resolution and sensitivity were realized in the prototype scanner.**

***Index Terms*—Angerdetector, animal imaging, GSO, high resolution, high sensitivity, large-axial FOV, PET imaging.**

I. Introduction

OVER the past several years, PET imaging has successfully demonstrated the capability to produce *in vivo* bio-distribution studies of small animals [1]–[5]. The advantage PET has over the traditional radio-nuclide labeling techniques are the reduction in time, effort, and sacrifice of animals to obtain statistically relevant data over varying physiological time periods. Additionally, it provides the capability to measure the metabolic activity of different organs in their natural state. The number and types of investigations being performed using PET in small animals is increasing [6]–[9]. Generally, one of its uses is in the study of transgenic animal models to understand the onset and development of diseases such as Parkinson's, Huntington's, and multiple sclerosis within humans. It has also found use in monitoring the delivery and expression of therapeutic genes used in gene therapy, as well as measuring changes in gene expression as a function of therapy or disease onset. Finally, PET imaging of small animals can also be used to develop more target specific PET tracers for use in clinical human imaging.

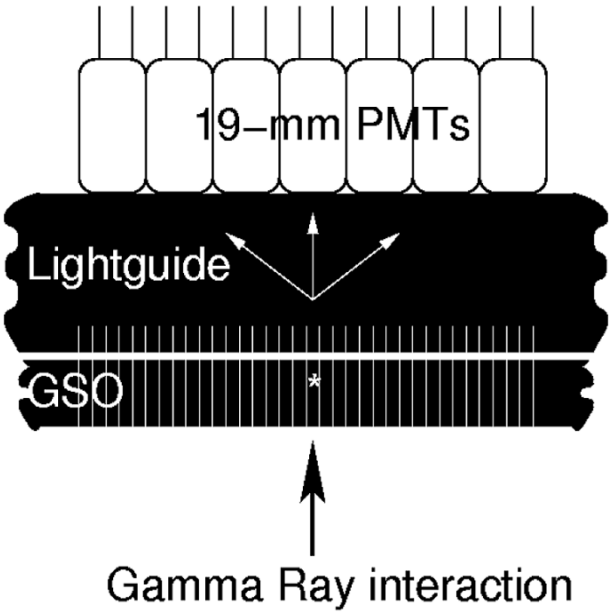

Fig. 1. GSO Anger logic detector using $2 \times 2 \times 10\ \mathrm{mm}^3$ crystals coupled to a continuous, slotted lightguide, and an array of 19 mm diameter PMTs. The lightguide thickness is 1.2 cm, and the slots are 0.5 cm deep.

In this work, we describe the development and evaluation of a new high resolution animal PET scanner (A-PET) using an Anger detector based on discrete GSO (gadolinium oxy-orthosilicate) crystals. The goal of this scanner design is to have good spatial resolution, high sensitivity, large axial field-of-view, low deadtime and good energy resolution. Since this scanner is being developed primarily for small animals, it is imperative to achieve close to 2 mm spatial resolution. Also, in order to image animals such as rats, as well as perform whole-body bio-distribution studies, a large axial field-of-view is required. The scanner field-of-view is designed to be large enough to accommodate the head of a cat or guinea pig, two animals commonly used in research. Three-dimensional imaging with a large axial field-of-view leads to high sensitivity, which is needed to successfully image new ligands with low radio-chemical yield or low specific activity. Finally, the contribution of scatter and random coincidences in the acquired image is significant even for small animals when performing volume imaging and, therefore, good system energy resolution is needed. Overall, our scanner design strives to achieve the

Manuscript received January 6, 2003; revised June 17, 2003. This work was supported by the U.S. Department of Energy Grant DE-FG02-88ER60642, and by the Small Animal Research program (SAIRP) at the University of Pennsylvania, Grant 1R24-CA83105-03.

S. Surti, J. S. Karp, and R. Freifelder are with the Department of Radiology, University of Pennsylvania, Philadelphia, PA 19104 USA (e-mail: surti@rad.upenn.edu).

A. E. Perkins and G. Muehllehner are with the Philips Medical Systems, Philadelphia, PA 19104 USA.

Digital Object Identifier 10.1109/TNS.2003.817950

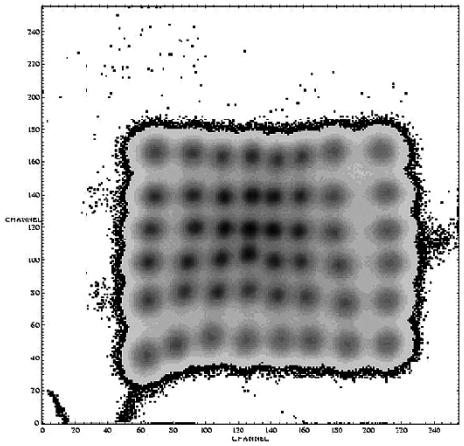

Fig. 2. Two-dimensional flood image obtained with a 511 keV photon source placed before a 48 crystal detector array coupled to a slotted lightguide.

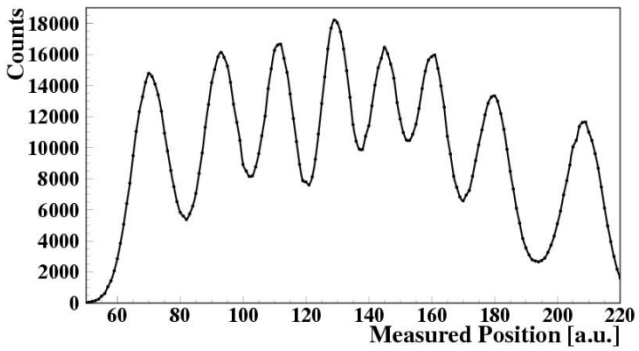

Fig. 3. One-dimensional profile drawn through the bottom row of crystals in the 2-D flood image shown in Fig. 2. We see good crystal separation with an average peak-to-valley ratio of 2.6.

abovementioned goals at a moderate cost and complexity such that it can be used by individual laboratories and investigators as a bench-top laboratory instrument.

II. Detector Design

Simulations were initially used in guiding the development of the GSO-based Anger-logic detector [10] using $2 \times 2 \times 10\ \mathrm{mm}^3$ crystals coupled to a continuous, slotted lightguide, and a hexagonally close-packed array of 19 mm diameter PMTs for signal readout (Fig. 1). A weighted local centroid algorithm [11] using a cluster of seven PMTS is used for position determination. Experimental measurements were first performed with a 48 crystal array using standard NIM and CAMAC electronics. The crystals were individually wrapped in five layers of teflon tape (pitch of 2.3 mm) before being arranged in an 8 $\times$ 6 grid on the lightguide and centered over a cluster of seven PMTs arranged hexagonally. Our experimental measurements show that best crystal discrimination is achieved by using a 1.2 cm thick lightguide with 0.5 cm deep slots (see Fig. 2). A 1-D profile drawn through row 6 of this flood image (Fig. 3) shows an average peak-to-valley ratio of 2.6. The use of GSO leads to a high scanner sensitivity with 10 mm thick crystal ($1/\mu = 1.5\ \mathrm{cm}$ for 511 keV photons), low scanner deadtime

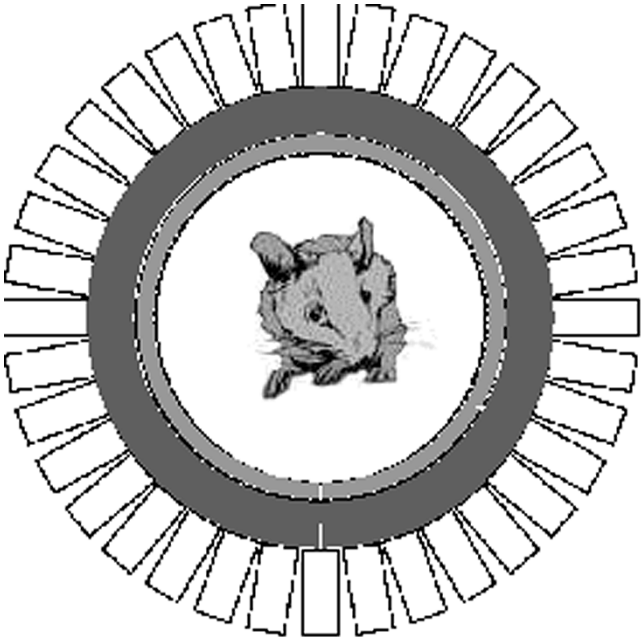

Fig. 4. A transverse schematic of the scanner showing the discrete GSO crystals glued to the inner surface of the annular lightguides and the PMTs on its outer surface.

(scintillator decay time, τ, is 85 ns for 0.5% Cerium doping), and uniform light output which leads to good system energy resolution. The Anger-logic detector achieves high spatial resolution due to the good crystal discrimination (2 mm crystals using 19 mm PMTs), and reduced scanner deadtime by restricting the scintillation light spread within a seven PMT cluster. For interactions in line with the center of a PMT, less than 1% of the emitted light goes beyond the cluster of PMTs (central plus six neighbors) that are used in position calculation. For events directly between two PMTs, the PMT with the larger signal and its six immediate neighbors are used to determine the interaction position. Here we observe a less than 20% decrease in total collected light as compared to events directly in line with the center of a PMT. The average energy resolution for all 48 crystals in Fig. 2 is 17% at 511 keV (worst energy resolution is 19% and best energy resolution is 15.5%).

III. Scanner Design

The scanner design utilizes a single annular lightguide 1.2 cm thick (with 0.5 cm deep slots), coupled with 16 680 $2 \times 2 \times 10\ \mathrm{mm}^3$ GSO crystals and an array of 288, 19 mm diameter PMTs. Due to its detector design that uses only 288 PMT and subsequent electronic channels, the A-PET is less complex than other animal specific PET scanners, leading to a cost-effective scanner design. The 10 mm long GSO crystals were chosen as a tradeoff between scanner sensitivity and parallax error in a small ring diameter. The crystal pitch is 2.3 mm leading to a packing efficiency of 75%. The lightguide size results in a scanner diameter of 21 cm (transverse field-of-view of 12.8 cm) with an axial length of 12.8 cm. The effective axial FOV is 11.6 cm in the final scanner design since we can resolve 50 rows of crystals. A transverse view of the scanner is shown in Fig. 4. This scanner will be operated exclusively in the 3-D volume imaging mode,

TABLE I
DIMENSIONS OF DIFFERENT CYLINDRICAL PHANTOMS USED IN SIMULATIONS

Phantom	Diameter (cm)	Length (cm)	Volume (mL)
Monkey head	8.9	6.1	380
Cat head	6.4	3.6	115
Rat body	5.1	10.9	220
Mouse body	3.7	6.8	70

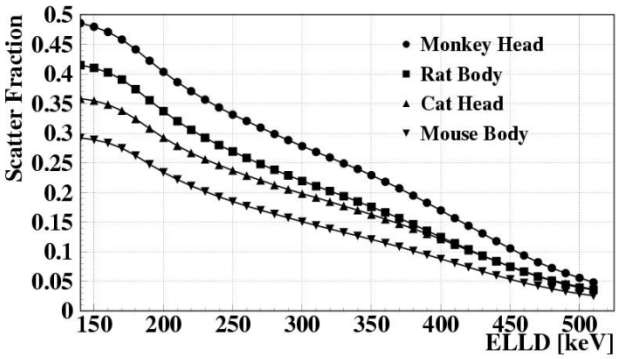

Fig. 5. Scatter fraction curves obtained through EGS4 simulation for four cylindrical phantoms within the A-PET scanner.

leading to about a 55% coverage of the total solid angle (in singles) for a point source at the center of the scanner field-of-view. As a result, based upon the geometry and crystal efficiency, we calculate a coincidence sensitivity of 1.3% for a point source when gating on photopeak events at 400 keV.

IV. SYSTEM SIMULATIONS

A. Scatter Fraction for Varying Cylindrical Phantom Sizes

We have performed EGS4 based scanner simulations [12] to study the scatter fraction, SF, in this scanner as a function of the lower energy gate (energy lower level discriminator, or ELLD). The SF is as defined by NEMA where $\mathrm{SF} = (\mathrm{Sc})/(\mathrm{T} + \mathrm{Sc})$ and T and Sc are true and scattered counts, respectively. These simulations assumed an energy resolution of 17% at 511 keV which is what we measured with our GSO detector described earlier. Four different cylindrical phantoms were studied and their dimensions are given in Table I. The results are shown in Fig. 5. These results show that a high ELLD value leads to low scatter fraction values. Overall, with an ELLD value of 400 keV, we see that scatter ranges from 17% for large phantoms (such as the monkey head) to 10% for the mouse phantom.

B. Impact of Energy Resolution on Scanner Performance

The above discussion implies that to reduce scatter events in the image the ELLD value should be raised as high as possible. The signal-to-noise ratio for a PET image has been shown to be proportional to the noise equivalence count (NEC) rate of the scanner [13], where

$$\mathrm{NEC} = \frac{T \times T}{T + Sc + R} \tag{1}$$

(R is random count-rate). As can be seen from the definition of the NEC rate, a high NEC value can be obtained by raising the ELLD value which reduces scattered events. However, this

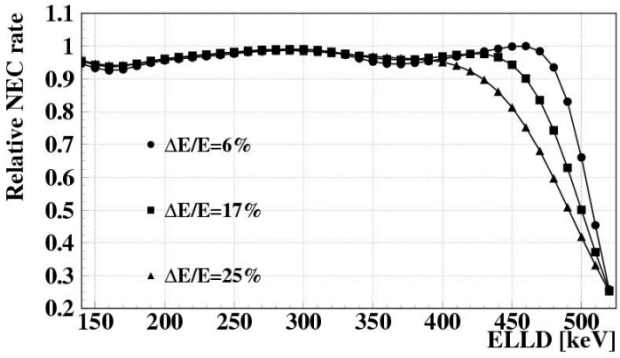

(a)

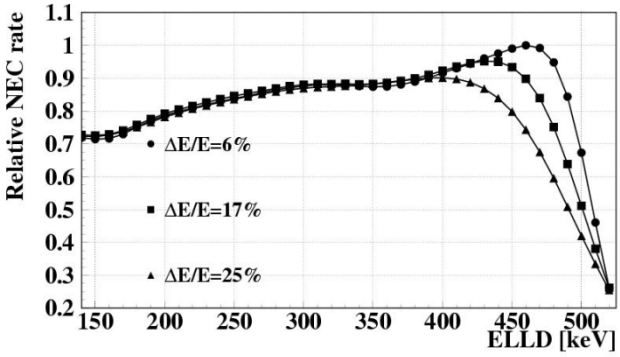

(b)

Fig. 6. Relative NEC rates as function of ELLD for the scanner with three different energy resolution. The top plot is for the smaller mouse body phantom, while the bottom plot is for the larger monkey head phantom.

also reduces the true count-rate in the scanner. Thus, there exists an optimum ELLD value at which the NEC rate peaks. All three types of coincidences (T, Sc, and R) are proportional to the square of the singles interaction efficiency (ϵ) of the scanner, which we can calculate from the energy spectrum obtained from the EGS4 simulation

$$T + Sc = k_1 \epsilon^2 A \tag{2}$$

$$R = k_2 \epsilon^2 A^2 \tag{3}$$

where A is the activity in the phantom, k_1 is a function of scanner and phantom geometry, while k_2 is a function of scanner and phantom geometry as well as the coincidence timing window. As a function of the ELLD, the NEC can then be shown to be

$$\begin{aligned}\mathrm{NEC(ELLD)} &= \frac{\left((1 - SF(\mathrm{ELLD})) \times k_1 \epsilon^2(\mathrm{ELLD}) A\right)^2}{k_1 \epsilon^2(\mathrm{ELLD}) A + k_2 \epsilon^2(\mathrm{ELLD}) A^2} \\ &= (1 - SF(\mathrm{ELLD}))^2 \times \epsilon^2(\mathrm{ELLD}) \\ &\quad \times \frac{k_1^2 A}{k_1 + k_2 A}. \end{aligned} \tag{4}$$

Thus

$$\mathrm{NEC(ELLD)} \propto (1 - \mathrm{SF(ELLD)})^2 \times \epsilon^2(\mathrm{ELLD}).$$

The proportionality factor will depend upon the scanner dead-time at a given count-rate as well as provide the absolute scaling factor for the NEC value as shown in (4). Using the energy spectra and SF from the EGS4 simulation, we calculated this relative NEC rate for the A-PET scanner as a function of ELLD

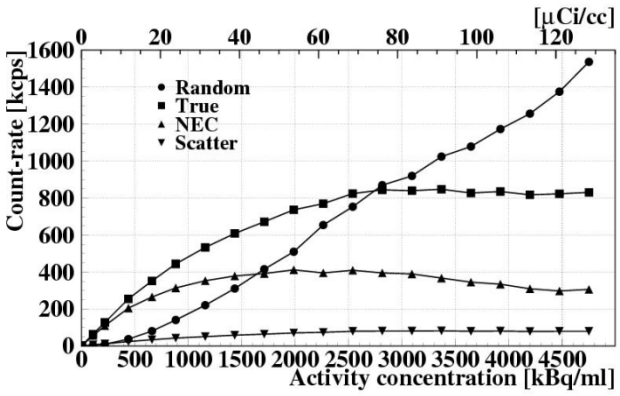

(a)

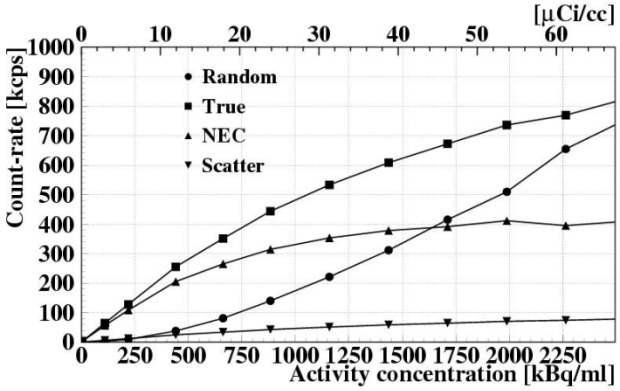

(b)

Fig. 7. Count-rate curves obtained through simulations for the cylindrical mouse phantom in the A-PET scanner. (a) Full count-rate curve, beyond peak NEC. (b) Expanded view for activity concentrations up to peak NEC.

for three different energy resolutions, 6%, 17%, and 25%. The 17% value represents what we measured for our GSO detector, while 25% is the general value for current animal PET systems with similar characteristics. The 6% energy resolution, however, represents an almost ideal detector with excellent energy resolution, and it is used as a standard to which other results can be compared. The results for the relative NEC calculation are shown in Fig. 6 for the small mouse body phantom (Top) and large monkey head phantom (Bottom). These results show that for imaging small animal such as mice, energy resolution does not significantly affect the NEC rate as long as the ELLD value is adjusted to achieve best results. However, for large animals such as a monkey, close to ideal energy resolution (6%) will lead to a 10% gain in the NEC rate for any given activity concentration.

C. Scanner Count-Rate Performance

We have also performed count-rate simulations (HCRSim) [14], [15] to evaluate the performance of the A-PET scanner in animal imaging situations using the previously described cylindrical phantoms. These Monte Carlo simulations perform a detailed analysis of pulse pileup in an Anger detector using the spatial spreading of the light within it, as well as the signal decay time for the scintillator. A triggering scheme which minimizes the deadtime for such a detector was employed, and effects of pulse pileup used to calculate the percentage of events which

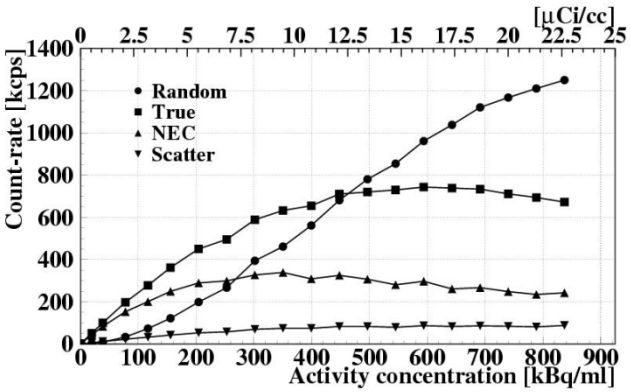

Fig. 8. Count-rate curves obtained through simulations for the cylindrical monkey head phantom in the A-PET scanner.

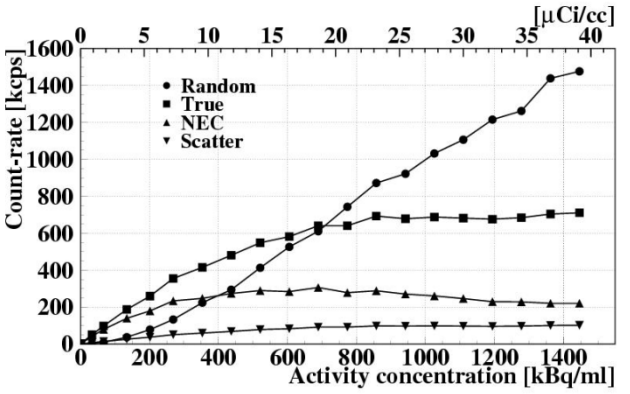

Fig. 9. Count-rate curves obtained through simulations for the cylindrical rat phantom in the A-PET scanner.

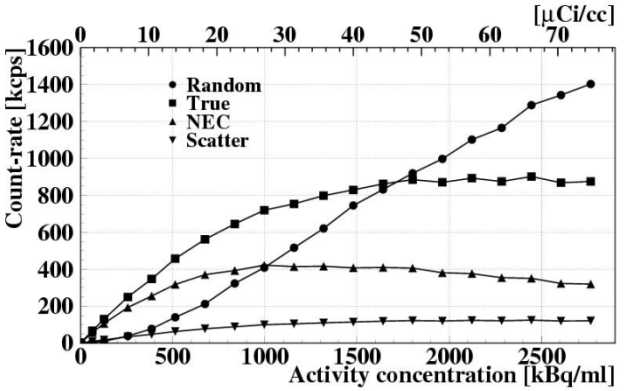

Fig. 10. Count-rate curves obtained through simulations for the cylindrical cat head phantom in the A-PET scanner.

fall outside energy window. The subsequent electronics were modeled after the original PENN-PET scanners [11] with a paralyzable deadtime. For these simulations an ELLD value of 400 keV was used. Figs. 7–10 show the count-rate curves obtained for all four phantoms. The true sensitivity of the A-PET scanner is 0.6 kcps/kBq/ml (22.2 $\mathrm{kcps}/\mu\mathrm{Ci}/\mathrm{cc}$) for the mouse body (smallest) phantom and 2.6 kcps/kBq/ml (96.2 $\mathrm{kcps}/\mu\mathrm{Ci}/\mathrm{cc}$) for the monkey head (largest) phantom. For example, injecting 1 mCi in a mouse will lead to a trues rate of $\sim$250 kcps. Therefore,

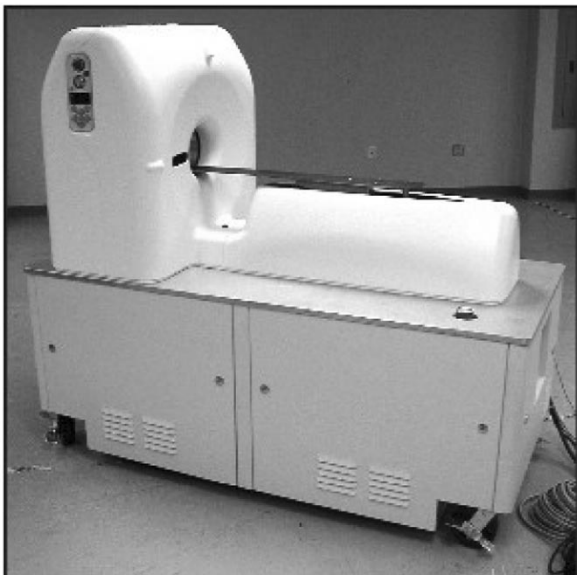

Fig. 11. A view of the completed A-PET scanner.

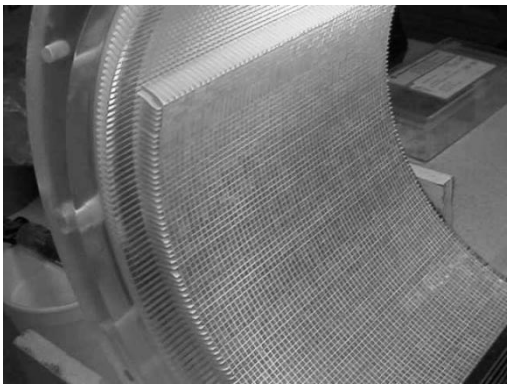

(a)

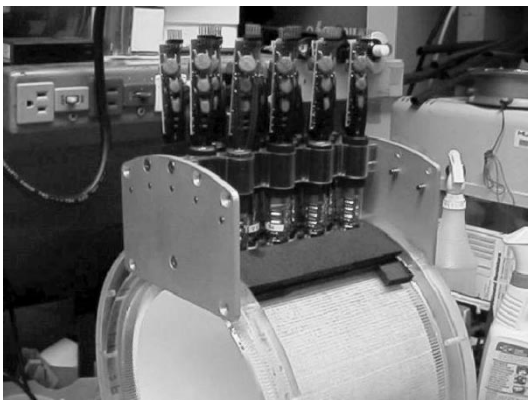

(b)

Fig. 12. Pictures of the A-PET lightguide with some of the 16 680 crystals glued to its inner surface as well as set of PMTs glued on the outer surface.

we will be able to use low activity injections to achieve high statistical quality in the images. Similarly, for primate imaging there is typically 3 mCi of activity present in the brain which implies a true coincidence rate of more than 200 kcps in the A-PET. It should be emphasized that these activity levels are for typical studies currently being performed at various institutions,

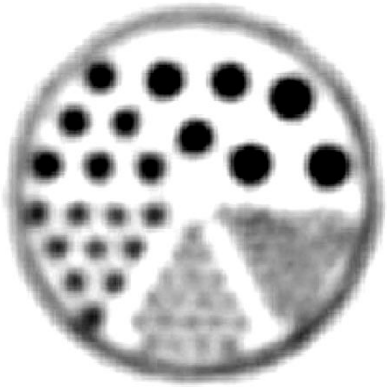

Fig. 13. A central slice from reconstructed image of a Micro Deluxe Phantom with hot rod inserts. The rod diameters in each of the six segments are 4.8, 4.0, 3.2, 2.4, 1.6, and 1.2 mm. The rod spacing is twice the rod diameter.

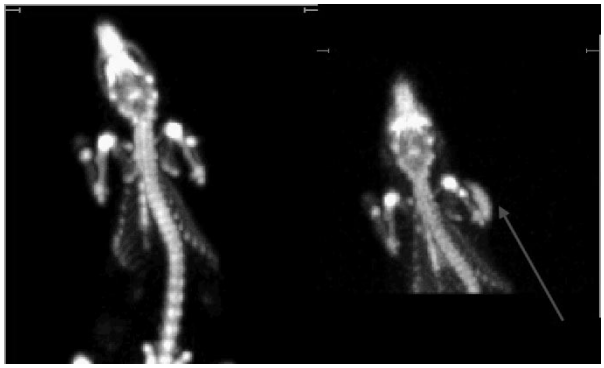

Fig. 14. An $^{18}\mathrm{F}$ bone scan (Left) of a 200 g male Fisher rat followed two hours later by an $^{18}\mathrm{F}-\mathrm{FDG}$ study (Right). In the $^{18}\mathrm{F}-\mathrm{FDG}$ study the subcutaneously implanted 9L glioma tumor is clearly visible as marked by the arrow.

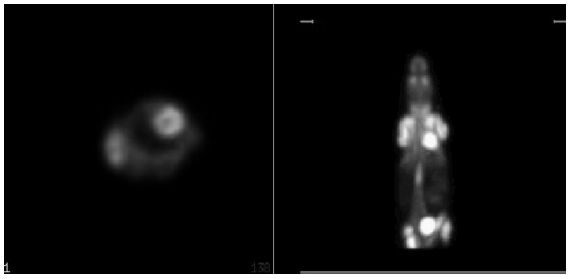

Fig. 15. An $^{18}\mathrm{F}-\mathrm{FDG}$ study of a 37 healthy male ICR mouse. On the left, we can see the $^{18}\mathrm{F}-\mathrm{FDG}$ uptake in the myocardium.

and do not exhaust all possible type of studies which will be performed on animal PET scanners. Future studies could very well involve injecting larger activity amounts in the animals. Since the A-PET peak NEC occurs at high activity levels, the scanner design provides the capability for its use in such situations.

V. Conclusion and Current Status

The A-PET scanner was recently completed. The scanner in its gantry and associated bed can be seen in Fig. 11. Fig. 12 shows the scanner at earlier stages of construction with a partial bank of glued crystals and PMTs. Initial calibrations, performance tests, and animal studies have been completed. These

results are promising and a more thorough system evaluation is ongoing. The spatial resolution of the scanner near the center was measured to be 2.26 mm with ^{18}F. At a radial position of 6 cm, the spatial resolution shows small degradation due to depth-of-interaction effects, increasing to 3.2 mm. We have also measured the absolute sensitivity of the scanner using a small ^{22}Na source placed in the center of the FOV. The absolute sensitivity was measured to be 1.3% in agreement with our calculated value. We also measured the absolute sensitivity of the scanner using a line source with varying number of aluminum sleeves, a technique originally described by Bailey [16] and more recently defined by NEMA as the standard way to measure sensitivity of PET systems [17]. This measurement gave an absolute sensitivity of 5.45 cps/kBq after normalizing for activity within the 11.6 cm axial FOV. Fig. 13 shows an image acquired with a 4.5 cm diameter, 3.7 cm long cylinder with hot rod inserts (Micro Deluxe Phantom, Data Spectrum Corporation). The rod diameters are 4.8, 4.0, 3.2, 2.4, 1.6, and 1.2 mm with a rod spacing of twice the rod diameter. The 2.4 mm rods are very clearly visible, while one could also mark the edges of the 1.6 mm rods. This result is consistent with the spatial resolution of the scanner and demonstrates very good uniformity and image quality. We have also performed some initial animal studies on this scanner. Fig. 14 (left) shows an ^{18}F bone scan of a 200 g male Fisher rat. The rat was injected with 0.5 mCi of ^{18}F and scanned one hour after injection. This image was acquired with two bed positions with a 50% bed overlap. The scan time was 15 min per bed position. The skeletal structure is well delineated, with the vertebra in the spine distinguished. Fig. 14 Right shows the same rat imaged 2 h after the ^{18}F scan, now using $^{18}\mathrm{F}-\mathrm{FDG}$. This rat was subcutaneously implanted with a 9L glioma tumor 11 days before these studies were performed. The $^{18}\mathrm{F}-\mathrm{FDG}$ scan was performed after injection of 0.7 mCi, and data acquired for a single bed position with an acquisition time of 15 min. The $^{18}\mathrm{F}-\mathrm{FDG}$ scan clearly shows the $^{18}\mathrm{F}-\mathrm{FDG}$ accumulation in the right hand shoulder where the tumor was implanted. Fig. 15 shows an $^{18}\mathrm{F}-\mathrm{FDG}$ scan of a 37 g healthy male ICR mouse. The mouse was injected with 0.6 mCi of $^{18}\mathrm{F}-\mathrm{FDG}$ in a 200 μL solution, and scanned 1 hr after injection. This image was acquired with a single 15 min bed position, and one can easily visualize the $^{18}\mathrm{F}-\mathrm{FDG}$ uptake in the heart. All these studies were reconstructed with 3-D RAMLA iterative reconstruction [18], after direct online randoms subtraction and normalization of the acquired sinograms. In the next couple of months, we anticipate finishing scanner calibrations for transmission and scatter correction, thereby producing fully corrected, quantitative imaging studies. For scatter correction we currently have the option of a 2-D tail-fitting technique as well as a model-based single scatter simulation [19] adapted for the animal scanner. For transmission scanning, we currently use a rotating 5 mCi ^{137}Cs source placed within the FOV. For two emission bed positions, four separate transmission scans are required with a total scan time of 3 min. The acquired transmission data set is then rebinned using either SSRB [20] or FORE into 2-D sinograms followed by iterative reconstruction with OSEM [21]. We are also investigating the possibility of keeping the transmission source outside the FOV, and using cone-beam reconstruction techniques for producing reconstructed transmission images with a single rotating source position. The transmission image will then be segmented using a histogram thresholding technique [22] to identify the tissue.

It needs to be emphasized that these are initial results and we have not yet optimized the imaging protocols or data processing. Thus, we expect further improvements in image quality once these steps are taken. We will also perform a detailed series of performance evaluation measurements to fully characterize the scanner. Spatial resolution of 2.3 mm will allow the possibility to quantitate tumor uptake and image organs in small animals such as the mouse heart. The large FOV of the A-PET leads to a high sensitivity scanner, thus providing the capability to image low specific activity ligands, as well as perform whole-body bio-distribution studies with one bed position. We achieve these performance characteristics while keeping the scanner design simple and cost-effective.

ACKNOWLEDGMENT

The authors would like to thank P. Acton, S. Evans, C. Hou, C. Koch, and L. Shuman for help with the animal studies. In addition, C. Cardi, M. Daube-Witherspoon, and M. Werner provided invaluable help with the completion, and eventual data collection of this scanner. Finally, they would like to thank the Engineering Group, Philips Medical Systems, Philadelphia, PA, for their collaboration and support in the design and construction of this scanner.

REFERENCES

[1] R. Lecomte, J. Cadorette, and S. Rodrigue *et al.*, "Initial results from the Sherbrooke avalanche photodiode positron tomograph," *IEEE Trans. Nucl. Sci.*, vol. 43, pp. 1952–1957, June 1996.

[2] A. P. Jeavons, R. A. Chandler, and C. A. R. Dettmar, "A 3-D HIDAC-PET camera with submillimeter resolution for imaging small animals," *IEEE Trans. Nucl. Sci.*, vol. 46, pp. 468–473, June 1999.

[3] A. F. Chatziioannou, S. R. Cherry, and Y. P. Shao *et al.*, "Performance evaluation of micro PET: a high-resolution lutetium oxyorthosilicate PET scanner for animal imaging," *J. Nucl. Med.*, vol. 40, no. 7, pp. 1164–1175, July 1999.

[4] S. I. Ziegler, B. J. Pichler, and G. Boening *et al.*, "A prototype high-resolution animal positron tomograph with avalanche photodiode arrays and LSO crystals," *Eur. J. Nucl. Med.*, vol. 28, no. 2, pp. 136–143, 2001.

[5] Y. C. Tai, A. Chatziioannou, and S. Siegel *et al.*, "Performance evaluation of the microPET P4: a PET system dedicated to animal imaging," *Phys. Med. Biol.*, vol. 46, no. 7, pp. 1845–1862, July 2001.

[6] S. S. Gambhir, J. R. Barrio, and L. Wu *et al.*, "Imaging of adenoviral-directed herpes simplex virus type 1 thymidine kinase reporter gene expression in mice with radiolabeled ganciclovir," *J. Nucl. Med.*, vol. 39, no. 11, pp. 2003–2011, Nov. 1998.

[7] S. Hume and T. Jones, "Positron emission tomography (PET) methodology for small animals and its application in radiopharmaceutical preclinical investigation," *Nucl. Med. Biol.*, vol. 25, pp. 729–732, 1999.

[8] M. E. Phelps, "PET: the merging of biology and imaging into molecular imaging," *J. Nucl. Med.*, vol. 41, pp. 661–681, 2000.

[9] H. I. Kornblum, D. M. Araujo, and A. J. Annala *et al.*, "In vivo imaging of neuronal activation and plasticity in the rat brain by high resolution positron emission tomography (microPET)," *Nat. Biotechnol.*, vol. 18, no. 6, pp. 655–660, June 2000.

[10] S. Surti, J. S. Karp, R. Freifelder, and F. Liu, "Optimizing the performance of a PET detector using discrete GSO crystals on a continuous lightguide," *IEEE Trans. Nucl. Sci.*, vol. 47, pp. 1030–1036, June 2000.

[11] J. S. Karp, G. Muehllehner, D. Beerbohm, and D. Mankoff, "Event localization in a continuous scintillation detector using digital processing," *IEEE Trans. Nucl. Sci.*, vol. NS-33, pp. 550–555, Feb. 1986.

[12] L.-E. Adam, J. S. Karp, and G. Brix, "Investigation of scattered radiation in 3D whole-body positron emission tomography using Monte Carlo simulations," *Phys. Med. Biol.*, vol. 44, pp. 2879–2895, 1999.

[13] S. C. Strother, M. E. Casey, and E. J. Hoffmann, "Measuring PET scanner sensitivity: relating countrates to image signal-to-noise ratios using noise equivalent counts," *IEEE Trans. Nucl. Sci.*, vol. 37, pp. 783–788, Apr. 1990.

[14] D. A. Mankoff, G. Muehllehner, and J. S. Karp, "The high countrate performance of a two-dimensionally position-sensitive detector for positron emission tomography," *Phys. Med. Biol.*, vol. 34, pp. 437–456, 1989.

[15] S. Surti, "A Model of Scintillation Detector Performance for Positron Emission Tomography," Ph.D. dissertation, Univ. Pennsylvania, Philadelphia, PA, Dec. 2000.

[16] D. L. Bailey, T. Jones, and T. J. Spinks, "A method for measuring the absolute sensitivity of positron emission tomographic scanners," *Eur. J. Nucl. Med.*, vol. 18, pp. 374–379, 1991.

[17] NEMA, NEMA Standards Pub. NU 2-2001, NEMA, Rosslyn, VA, 2001.

[18] M. E. Daube-Witherspoon, S. Matej, J. S. Karp, and R. M. Lewitt, "Application of the row action maximum likelihood algorithm with spherical basis functions to clinical PET imaging," *IEEE Trans. Nucl. Sci.*, vol. 48, pp. 24–30, Feb. 2001.

[19] R. Accorsi, L.-E. Adam, M. E. Werner, and J. S. Karp, "Implementation of a single scatter simulation algorithm for 3D PET: Application to emission and transmission scanning," in *Proc. IEEE MIC Conf. Rec.*, San Diego, CA, 2002.

[20] M. E. Daube-Witherspoon and G. Muehllehner, "Treatment of axial data in three-dimensional PET," *J. Nucl. Med.*, vol. 28, pp. 1717–1724, 1987.

[21] J. S. Karp, A. J. Becher, and S. Matej, "Data processing and image reconstruction methods for the HEAD PENN-PET scanner," *IEEE Trans. Nucl. Sci.*, vol. 45, pp. 1144–1151, June 1998.

[22] K. Bilger, L.-E. Adam, and J. S. Karp, "Segmented attenuation correction using Cs-137 single photon transmission," in *Proc. IEEE MIC Conf. Rec.*, San Diego, CA, 2002.